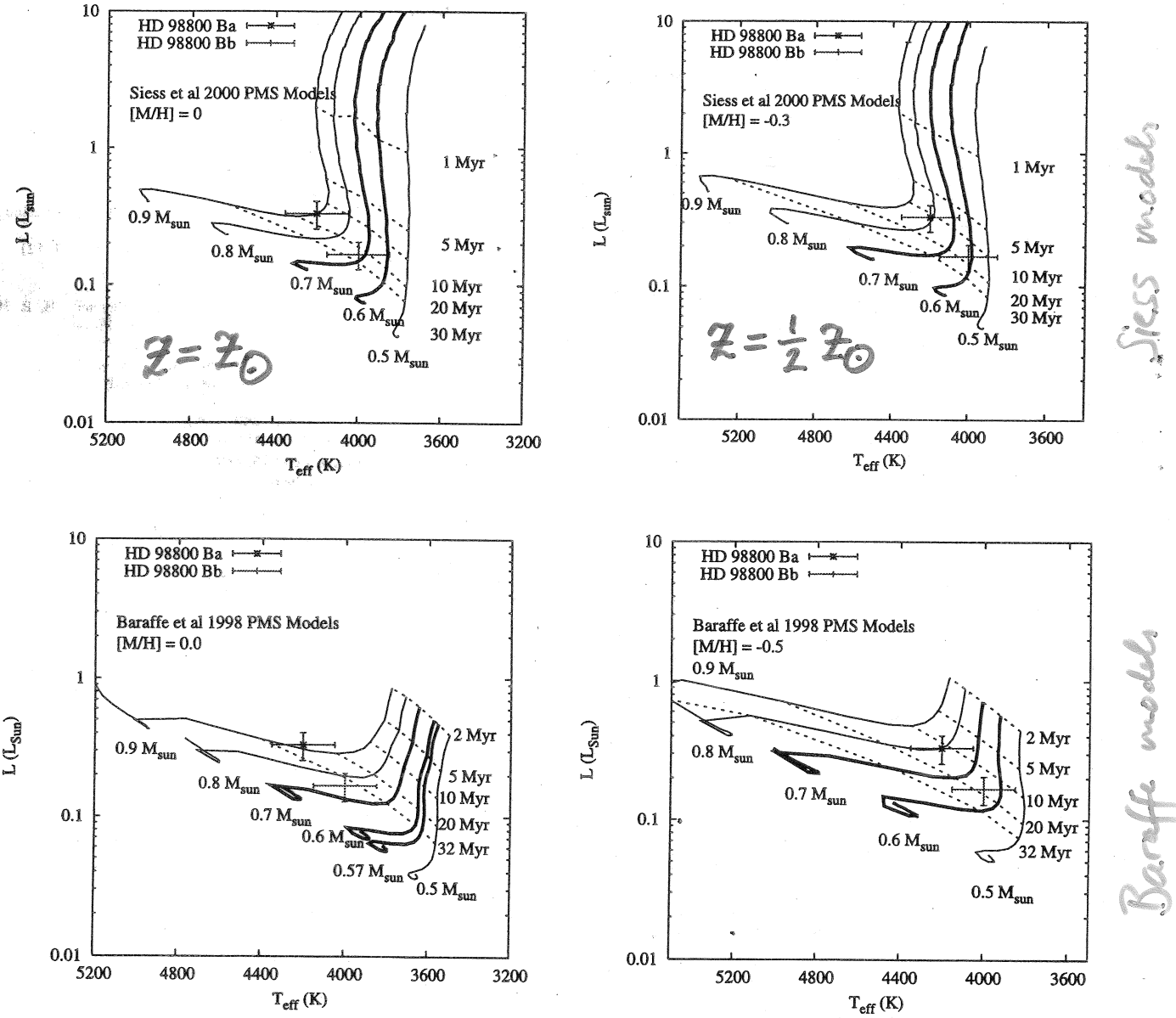

FIG. 6.—HD 98800 B components compared with PMS models. Here we show the HD 98800 B components in luminosity/$T_{\rm eff}$ space and PMS evolutionary tracks by Siess et al. (2000, *top*) and Baraffe et al. (1998, *bottom*). As found by P01, solar abundance models (*left*) suggest higher masses for the HD 98800 B than our orbit yields; however, a lower abundance ([M/H] = −0.3 to −0.5, *right*) for the components brings the inferred masses and radiative properties into better agreement with model predictions from both families. In all panels bold lines emphasize mass tracks bracketing component mass values implied by the orbit model (Table 5), and isochrones spanning a range of ages between 1 and 32 Myr are given.

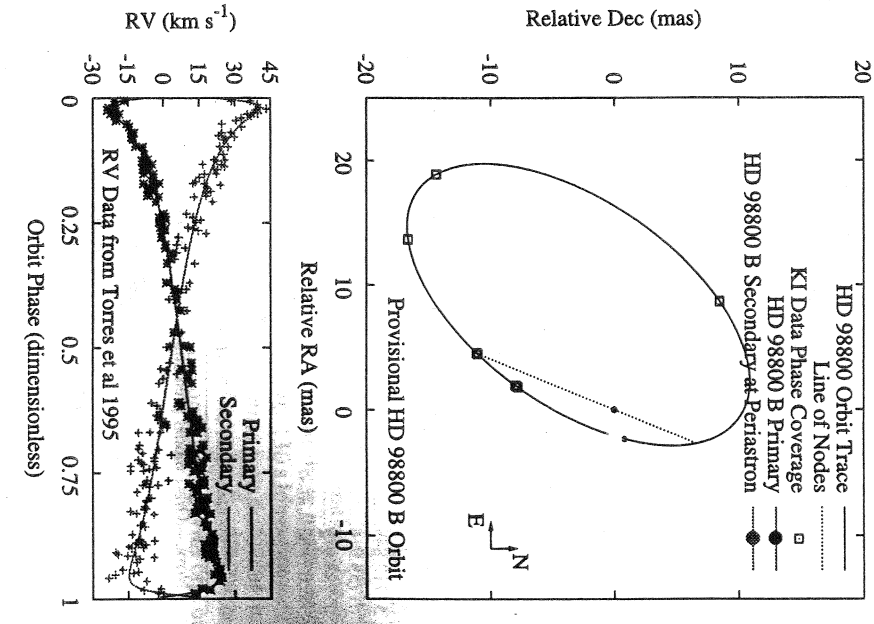

FIG. 1.—Orbit of HD 98800 B as derived in our joint-fit solution (Table 4). *Top*: Relative visual orbit model of HD 98800 B, with the primary and secondary objects rendered at T_0 (periastron). The specific epochs where we have KI I'^2 phase coverage are indicated on the relative orbit (they are not separation vector estimates). Component diameter values are estimated and rendered to scale. *Bottom*: Double-lined RV orbit model and data from Torres et al. (1995).

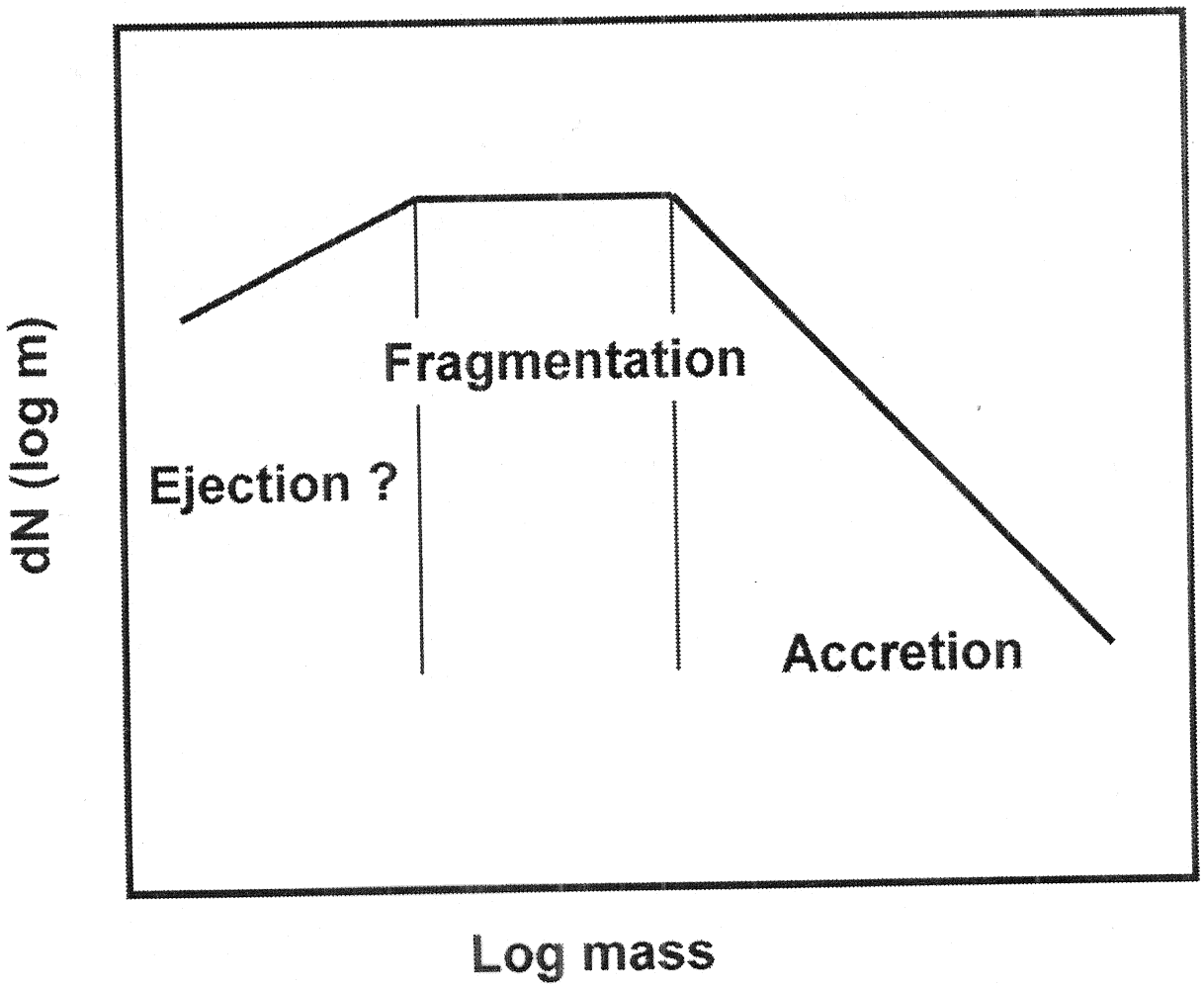

Fig. 11. A schematic IMF showing the regions that are expected to be due to the individual processes. The peak of the IMF and the characteristic stellar mass are believed to be due to gravita-

problematic as the core
does not appear to be ur
2006). Furthermore, the
cores generated from tu
be found in low stellar
dense cores of stellar c
close, or even relatively
the ability of the cluster
onto the stars in the clu
for more massive stars
mation. Continuing accr
massive stars in a form
settle, and remain, in th
produces the observed
clusters. The strong ma
($\propto M^2$) results in a Sal

Continued accretion
potentially explain the
the dependency of bina
et al., 2002b; *Bonnell*

the basic physical variable is the stellar mass. Note also that astronomers sometimes use, in place of $L_{\rm bol}$, the *bolometric magnitude*:

$$M_{\rm bol} \equiv -2.5 \log \left(\frac{L_{\rm bol}}{L_\odot} \right) + m_\circ \ , \tag{1.7}$$

where the constant $m_\circ$ is +4.75. The difference $M_{\rm bol} - M_V$ for a main-sequence star of any spectral type is known as the *bolometric correction*, here evaluated in the V-waveband.

Table 1.1 Properties of the Main Sequence

Mass ($M_\odot$)	Sp. Type	M_V (mag)	$\log L_{\rm bol}$ ($L_\odot$)	$\log T_{\rm eff}$ (K)	$t_{\rm MS}$ (yr)
60	O5	−5.7	5.90	4.65	3.4×10^6
40	O6	−5.5	5.62	4.61	4.3×10^6
20	O9	−4.5	4.99	4.52	8.1×10^6
18	B0	−4.0	4.72	4.49	1.2×10^7
10	B2	−2.4	3.76	4.34	2.6×10^7
8	B3	−1.6	3.28	4.27	3.3×10^7
6	B5	−1.2	2.92	4.19	6.1×10^7
4	B8	−0.2	2.26	4.08	1.6×10^8
2	A5	1.9	1.15	3.91	1.1×10^9
1.5	F2	3.6	0.46	3.84	2.7×10^9
1	G2	4.7	0.04	3.77	1.0×10^{10}
0.8	K0	6.5	−0.55	3.66	2.5×10^{10}
0.6	K7	8.6	−1.10	3.59	
0.4	M2	10.5	−1.78	3.54	
0.2	M5	12.2	−2.05	3.52	
0.1	M7	14.6	−2.60	3.46	

1.3.4 Consumption of Nuclear Fuel

Stars remain on the main sequence for relatively long periods of time because of the vast supply of hydrogen available for fusion. To estimate the main-sequence lifetime $t_{\rm ms}$, we use the fact that the basic nuclear reaction is the fusion of four protons into ^{4}He. This process releases 26.7 MeV per helium nucleus, or $0.007\, m_p\, c^2$ for each proton of mass m_p. If f_H is the fraction of hydrogen consumed, then the star releases a total energy

$$E_{\rm tot} = 0.007\, f_H\, X\, M_*\, c^2 \tag{1.8}$$

during this period. Here, X is the star's mass fraction in hydrogen, which is typically 70 percent. The energy $E_{\rm tot}$ divided by $t_{\rm ms}$ must equal the (nearly constant) luminosity L_*. Detailed

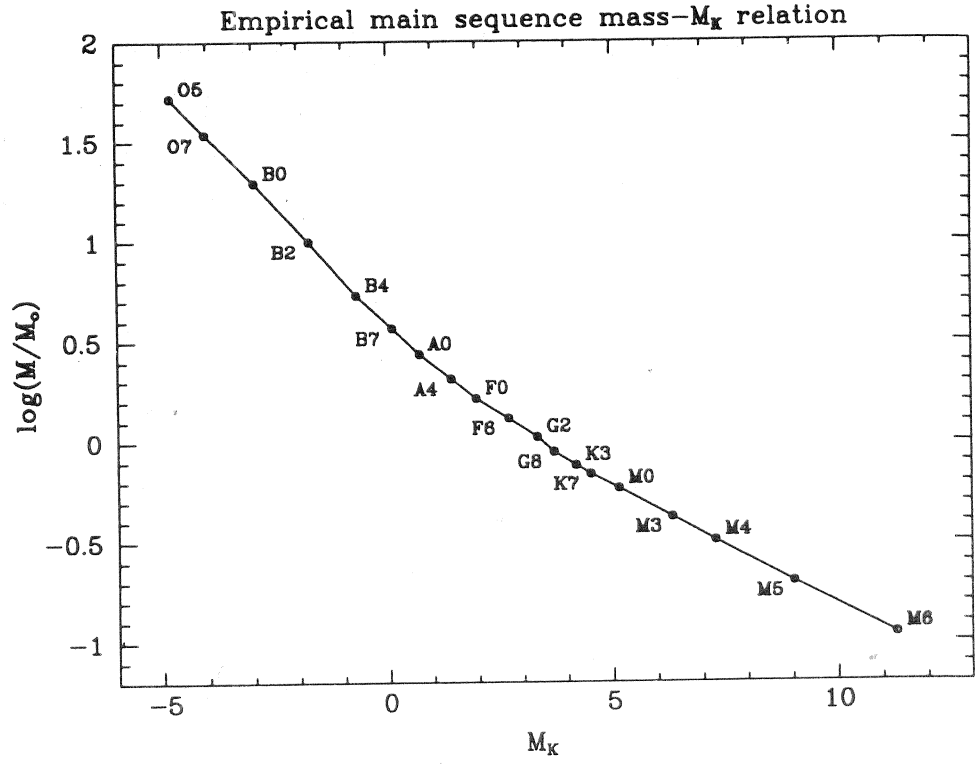

Figure 3. An empirical mass–M_K luminosity relation for main-sequence derived from the data of Miller and Scalo (1979), and Koornneef (1983*b*), foll Straw et al. (1989). Corresponding spectral types are also marked. It should be that there is considerable uncertainty in this relation for spectral types K0 anc as seen when compared to other empirical determinations (M. Simon, pe communication; Henry 1991).

present age of the coeval cluster in question), there is a kink in the luminosity relation. This leads to an increase in the value of d log M/dK a boost in the luminosity function at the corresponding K magnitude, cr

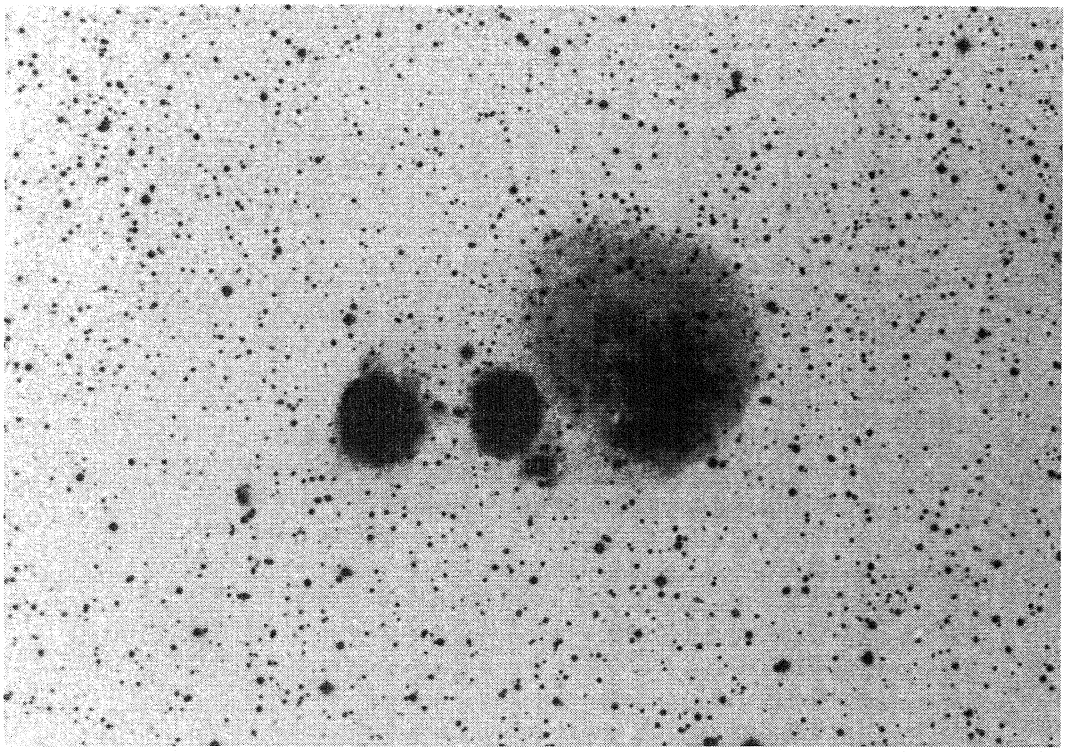

Plate 3 Negative optical photograph of three HII regions in the Gem OB1 association. The regions span a total distance of 9 pc.

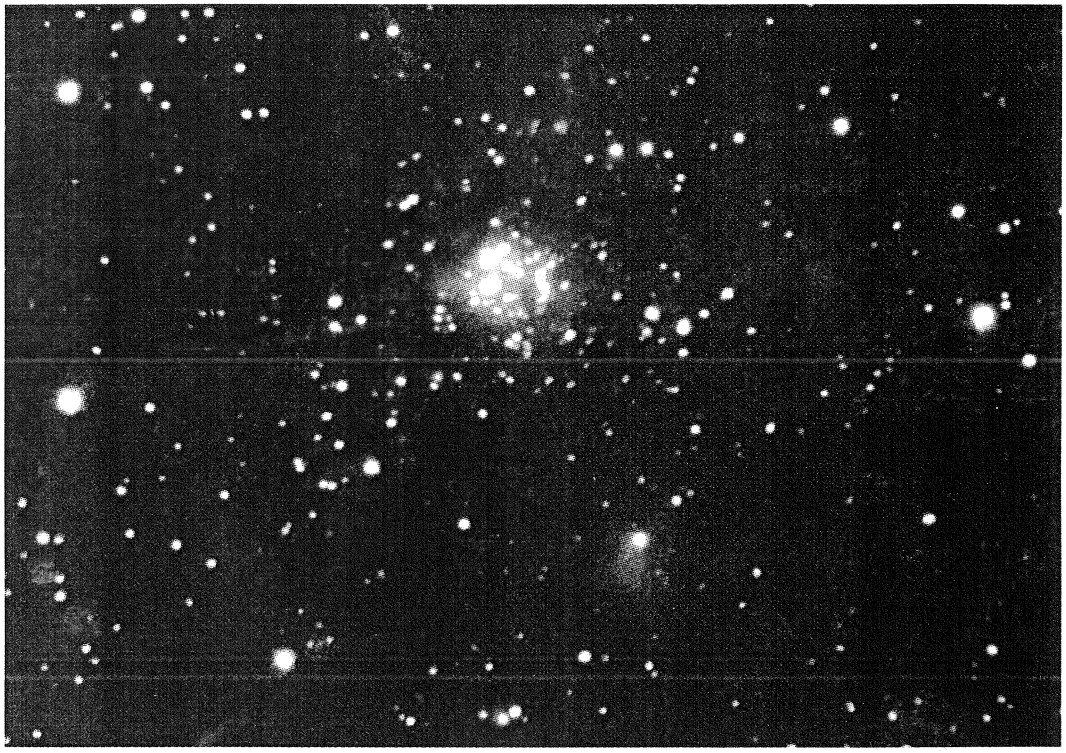

Plate 4 Expanded near-infrared (J, H, and K) image of Gem OB1. The bright nebula in the center lies between the left and center HII regions of Plate 3, and is invisible optically.

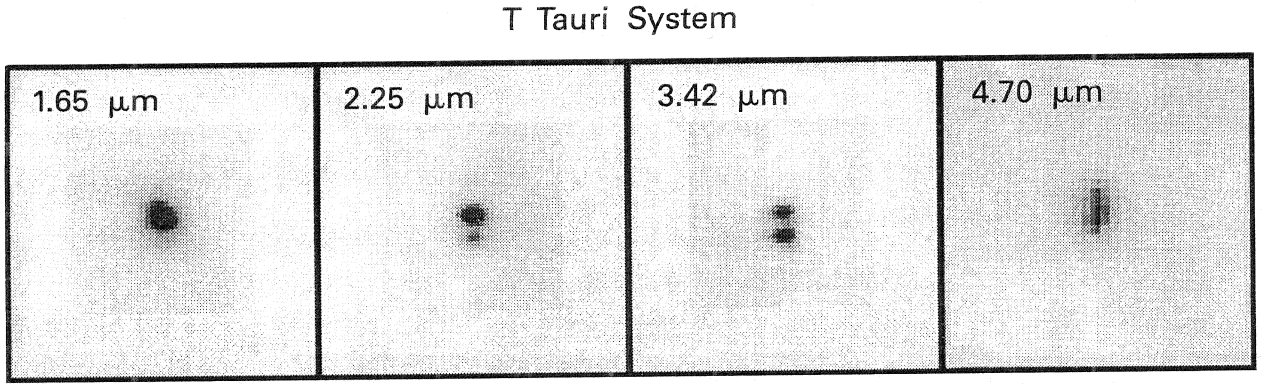

Figure 12.10 Near-infrared array observations of the T Tauri binary system. Each frame is an image at the indicated wavelength. The lower source is actually a tight binary, unresolved here.

Taurus-Auriga, composed of two solar-mass stars. If, as we shall verify, the period distribution for such systems resembles that of the dwarfs, then our example is likely to be a visual binary with a period of roughly 200 yr. From equation (12.15), $a_{\rm tot}$ would then be about 40 AU, or $0\farcs4$ at the Taurus-Auriga distance of 150 pc. Achieving this spatial resolution is technically challenging.

Another difficulty stems from the fact that the emitted flux from most pre-main-sequence stars is highest in the near infrared. Optical instruments, while still useful, are therefore not ideally suited for systematic observations. A significant advance in this regard has been the introduction of near-infrared arrays. We saw in Chapter 4 how these detectors revolutionized the study of embedded clusters. The arrays have also led to the discovery of a large number of close companions to T Tauri stars, ranging in angular separation from about $0\farcs7$ to $15''$. On a statistical basis alone, most of these systems must be pre-main-sequence binaries, rather than chance superpositions in the plane of the sky. Observers have been able to measure relative proper motions for some pairs; the calculated speeds appear to be consistent with those expected for gravitationally bound systems.

Figure 12.10 illustrates dramatically the power of near-infrared observations for revealing